Article

Volume and Nutrient Transports Disturbed by the Typhoon Chebi (2013) in the Upwelling Zone East of Hainan Island, China

Manli Zheng [1,2] iD **, Lingling Xie** [1,3,*] **, Quanan Zheng** [4] **, Mingming Li** [1,3] iD **, Fajin Chen** [1,3] iD **and Junyi Li** [1,3]

[1] Laboratory of Coastal Ocean Variation and Disaster Prediction, College of Ocean and Meteorology, Guangdong Ocean University, Zhanjiang 524088, China; zml07@scsio.ac.cn (M.Z.); limm@gdou.edu.cn (M.L.); fjchen@gdou.edu.cn (F.C.); jyl@gdou.edu.cn (J.L.)

[2] State Key Laboratory of Tropical Oceanography, South China Sea Institute of Oceanology, Chinese Academy of Sciences, Guangzhou 510000, China

[3] Key Laboratory of Climate, Resources, and Environment in Continental Shelf Sea and Deep Ocean, Guangdong Ocean University, Zhanjiang 524088, China

[4] Department of Atmospheric and Oceanic Science, University of Maryland, College Park, MD 20742, USA; qzheng2@umd.edu

* Correspondence: xiell@gdou.edu.cn

Abstract: Using cruise observations before and after the typhoon Chebi in August 2013 and those without the typhoon in July 2012, this study investigates variations in current structure, nutrient distribution, and transports disturbed by a typhoon in a typical coastal upwelling zone east of Hainan Island in the northwestern South China Sea. The results show that along-shore northeastward flow dominates the coastal ocean with a volume transport of 0.64×10^6 m^3/s in the case without the typhoon. The flow reversed southwestward, with its volume transport halved before the typhoon passage. After the typhoon passage, the flow returned back northeastward except the upper layer in waters deeper than 50 m and the total volume transport decreased to 0.10×10^6 m^3/s. For the cross-shelf component, the flow kept shoreward, while transports crossing the 50 m isobath decreased from 0.25, 0.12 to 0.06×10^6 m^3/s in the case without the typhoon as well as before and after typhoon passage, respectively. For the along-shore/cross-shelf nutrient transports, SiO$_3^{2-}$ has the largest value of 866.13/632.74 μmol/s per unit area, NO$_3^-$ half of that, and PO$_4^{3-}$ and NO$_2^-$ one order smaller in the offshore water without the typhoon. The values dramatically decreased to about one-third for SiO$_3^{2-}$, NO$_3^-$, and PO$_4^{3-}$ after the typhoon, but changed little for NO$_2^-$. The disturbed wind field and associated Ekman flow and upwelling process may explain the variations in the current and nutrient transports after the typhoon.

Keywords: transport; nutrient; typhoon; shelf sea; South China Sea

1. Introduction

The shelf sea, usually referring to the water region within the 200 m isobath, is an important oceanic area where the interactions between the sea and the land, as well as the exchange of substance and energy between near-shore waters and the deep ocean, are active [1–4]. Although the shelf sea occupies only 8% of the ocean area, it contributes 15–30% of the global marine primary productivity [5,6]. Therefore, it is closely related to human survival and development.

Cross-shelf transport is crucial for the geochemical processes in the shelf sea and the interaction between near-shore waters and the deep ocean [7]. It directly affects the ecosystems of offshore waters and the self-purification ability of the marine environment [7–10]. Thus, previous investigators have carried out research on cross-shelf transport using different methods [11–14]. Based on numerical simulations, Dinniman and Klinck [15] calculated the cross-shelf transports of the volume and nutrients at the shelf break of Ross Sea. They

obtained the values of 0.3×10^6 m^3/s and 7.1 kmol/s for volume and nutrient transports, respectively, in the Ekman layer. By combining the observed nutrient data and the modeled flow, Dong et al. [16] calculated the volume and nutrient transports across the 200 m isobath in the northern South China Sea (SCS) in spring and obtained onshore fluxes of 0.44×10^6 m^3/s and 6.65 kmol/s, respectively. Wang et al. [17] analyzed the circulation and cross-shelf movements in the northern SCS based on the Princeton Ocean Model (POM) and the climatology data from the Generalized Digital Environment Model (GDEM, version 3.0). They found that the cross-shelf flow occupies 15–20% of the total flow, and the annually averaged volume transport across the 200 m isobath reaches 9.4×10^6 m^3/s. Liu et al. [18] used satellite altimeter data for calculating the seasonal and interannual cross-shelf volume fluxes in the northern SCS. The results have significant variations with the extreme values of $\pm 1 \times 10^6$ m^3/s for the cross-shelf transport and $\pm 2 \times 10^6$ m^3/s for along-shore transport.

The continental shelf east of Hainan Island is located in the northwestern SCS (Figure 1), where the slope is almost parallel to the northeast–southwestern coastline. The area is located within the East Asia monsoon zone. In winter, the northeasterly winds prevail, so that the coastal current is southwestward. In summer, southwesterly winds prevail and the coastal current is dominated by a northeastward flow. Meanwhile, the Ekman transport drives the summer coastal upwelling, resulting in an important fishery and biodiversity region in China [19–21]. Previous investigators have addressed the physical and chemical characteristics of circulation and nutrients, as well as variation mechanisms in this area, especially during the upwelling period in summer [13,22–25]. However, the research on quantitative calculation or estimates of the volume and nutrient transports, especially cross-shelf transports, still needs to be enhanced. Using the observations of current, temperature, and salinity in the winter of 2012, Zheng et al. [26] calculated cross-shelf fluxes of volume, heat, and salt, and the results are 0.56 m/s, 1.29×10^7 W/m^2, and 3.78×10^3 kg/s/m^2, respectively. Here, we investigate the along-shore and cross-shelf transports in the summer season.

Typhoons pass over the upwelling zone east of Hainan Island in summer every year. Affected by typhoons, the hydrological characteristics and current structure in the shelf sea may have dramatic changes [27–32]. When the typhoon intrudes the south of the upwelling region, the upwelling-favorable southwesterly could be suppressed by an anomalous northeasterly, which destroys the traditional coastal upwelling pattern. However, the upwelling system may recover within 1–2 days after the typhoon passage [33]. On the other hand, the rainfall brought by the typhoons increases the runoff from the land. The nutrient concentration of the sea water is increased by an order of magnitude, so that the concentration of chlorophyll a (Chl a) enhances [34–37]. Therefore, this study aims to answer the following questions: How does the typhoon affect the nutrient distribution of the continental shelf east of Hainan Island? What is the change in cross-shelf transport when a typhoon passes by?

These challenges motivate us to use cruise data of current velocities and nutrients, observed in July 2012 without the typhoon and in August 2013 during the typhoon, to calculate the cross-shelf and along-shore transports. This paper is organized as follows: The next section describes the cruise observation program and the data processing methods. Section 2 analyzes the difference between current and nutrient concentration before and after the typhoon. Section 4 gives the results of cross-shelf and along-shore transports of volume and nutrients. Sections 4 and 5 provide a discussion and the conclusions, respectively.
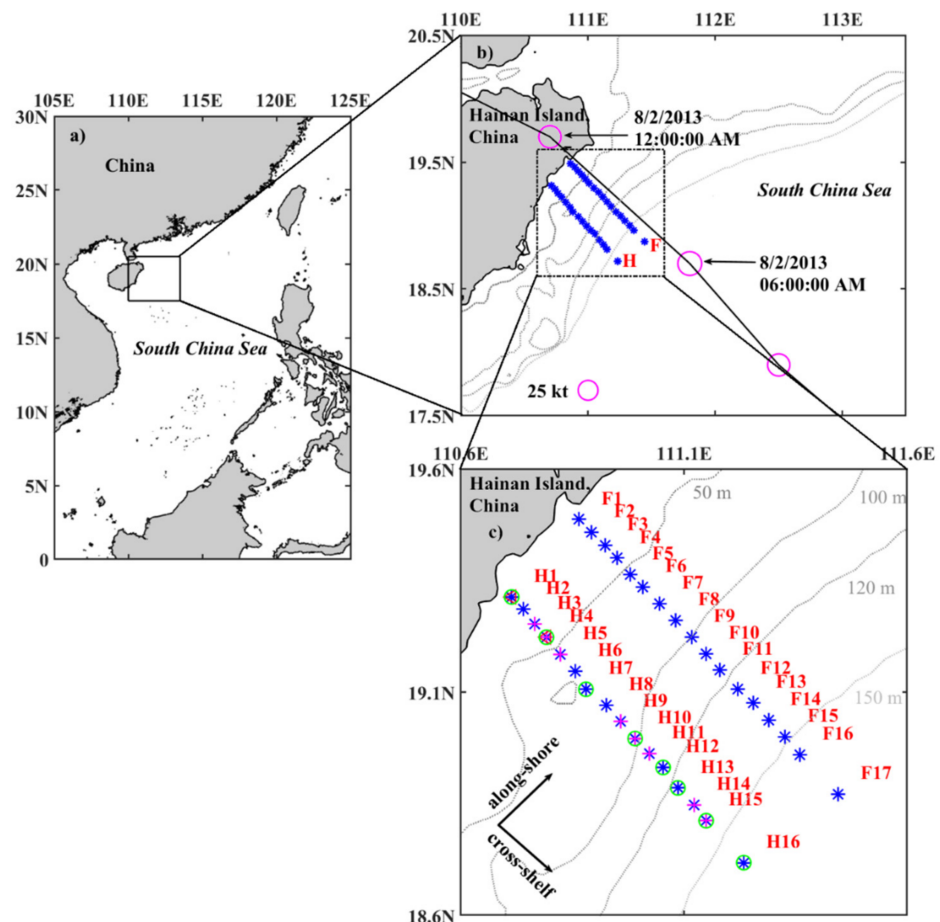
Figure 1. Map of the South China Sea (**a**), the study area with sections H and F (blue asterisks), and the ground path of the typhoon Chebi (2013) (black line with purple rings) (**b**). Purple rings represent the maximum wind speed of the typhoon. Cruise observation sections and stations are shown in panel (**c**), with station codes in red. Blue asterisks * represent the stations of the acoustic Doppler current profiler (ADCP). Pink pluses +, red triangles △, and green circles ○ represent the stations with water sampling in the cases without the typhoon, before the typhoon, and after the typhoon in section H, respectively. Gray lines represent isobaths of 50, 100, 120, and 150 m.

2. Materials and Methods

2.1. Study Area and Station Setting

As shown in Figure 1b, the cruise-surveyed region is located on the continental shelf east of Hainan Island in the northwestern SCS. It is a typical summer coastal upwelling region characterized by tropical cyclone passage. Joint physical and biogeochemical observations (Section 2.3) were conducted along two cross-shelf sections, H and F. There are 16 stations in section H and 17 in section F (Figure 1c), and the two sections are spaced apart by about 25 km. The stations are spaced apart by about 5 km within the 150 m isobath, and 10 km beyond the 150 m isobath.

2.2. Typhoon Chebi (2013)

Tropical cyclone Chebi (2013) formed in the central SCS on 31 July 2013 and moved along a north–northwestern path. During the movement, its intensity gradually increased. As shown in Figure 1b, the cyclone entered the study area at 6:00 a.m. on August 2 (Coordinated Universal Time—UTC), passing over the northeastern side of section F, and landed at northern Hainan Island around 12:00 at noon on August 2 (Figure 1b). It is worth noting that the typhoon spent 3.5 h to pass the upwelling region with the maximum wind speed of up to 30 m/s. Evidently, Chebi (2013) had a maximum sustained wind of 30 kt

before landfall and reached a strength of strong tropical storm (STS) with the minimum press of 980 hPa. After landfall, the maximum sustained wind gradually decreased [38,39]. In the following text, we refer to different categories of the tropical cyclones with the same name, "typhoon". The typhoon data were downloaded from the website of the Joint Typhoon Warning Center (JTWC) (https://www.metoc.navy.mil/jtwc/jtwc.html, accessed on 4 February 2021), including the typhoon intensity every 6 h, center position, center minimum barometric pressure, and maximum sustained wind.

2.3. Cruise Observation

The cruise observations were carried out twice in two years in different cases. In 2012, in situ observations in sections F and H were conducted on 13 and 15–18 July in calm weather without the typhoon (the case without the typhoon). In 2013, observations in section H were conducted on both 30 July–1 August before Chebi (2013) passage (the case before the typhoon) and 8–9 August after the typhoon passage (the case after the typhoon), while observations in section F were only conducted on 8–9 August in the case after the typhoon.

The horizontal velocity was measured with a 300 kHz acoustic Doppler current profiler (ADCP), manufactured by RD Instruments Inc. The resolution is 1 mm/s, and the accuracy is 1 cm/s. During observations, the bin size of the ADCP was set to 4 m and the time interval was 30 s. The ADCP was hung at about 2 m below the ocean surface on the windward side of the Research Vessel when it stopped and thus allowed continuous observations for 20 min.

The temperature, salinity, and depth were measured using the Seabird Electronic (SBE) 19 plus conductivity–temperature–depth (CTD) profiler. Meanwhile, water samples were taken from different layers from selected stations spaced, as shown in Figure 1c, by hydrophore. The water samples were immediately filtered through a 0.45 μm acetate membrane (the membrane was pre-soaked with 1:1 000 hydrochloric acid solution for 24 h, then washed with Milli-Q water to neutral), and the filtrate was placed in a 100 mL polyethylene bottle, stored frozen at $-20\,^{\circ}$C, and brought back to the onshore laboratory for nutrient determination. For Chl a, the water samples (500–1000 mL) were pre-filtered through a 200 μm sieve and then filtered through a glass fiber membrane (pore size 0.65 μm). About 1 mL magnesium carbonate suspension with a concentration of 10 g/dm^3 was 9added before filtration to prevent the removal of magnesium, stored at $-80\,^{\circ}$C, and brought back to the onshore laboratory for the determination of Chl a [40].

2.4. Wind Data

The reanalyzed sea surface wind data downloaded from the website of the European Centre for Medium-Range Weather Forecasts (ECMWF) (https://apps.ecmwf.int/datasets/data/interim-full-daily/levtype=sfc/, accessed on 4 February 2021) are used for wind analysis. The spatial resolution is $0.25^{\circ} \times 0.25^{\circ}$. The time interval is 3 h. The mean wind on each day is the average of eight samples on that day.

The Ekman layer depth, Ekman transport, and Ekman pumping are calculated with the ECMWF daily mean wind data using the following equations.

For the Ekman layer depth D_E,

$$D_E = 0.4 \times \sqrt{T/\rho_a}/f \tag{1}$$

For the Ekman transport M_{Ex} and M_{Ey},

$$\begin{cases} M_{Ex} = T_{yz}(0)/f \\ M_{Ey} = -T_{xz}(0)/f \end{cases} \tag{2}$$

For the Ekman pumping $w_E(0)$,

$$w_E(0) = -\frac{1}{\rho}\left(\frac{\partial M_{Ex}}{\partial x} + \frac{\partial M_{Ey}}{\partial y}\right) \tag{3}$$

where T is the wind stress ($T_{yz}(0)$ and $T_{xz}(0)$ are the components of surface wind stress), ρ_a is the air density, ρ is the sea water density, and f is the Coriolis parameter.

2.5. Velocity Data Process

2.5.1. Tidal Currents

To eliminate the tidal currents from the observed velocities, we use the OSU TOPEX/ Poseidon Global Inverse Solution (TPXO), which is a model of barotropic ocean tides created by Oregon State University [41]. The tidal constituents M2, S2, N2, K2, K1, and O1 at the observed stations are calculated from the model and then extracted from the observations.

2.5.2. Along-Shore and Cross-Shelf Currents

The current velocities are decomposed into the cross-shelf and the along-shore components v_c and v_a as

$$\begin{cases} v_c = u \times \cos\theta - v \times \sin\theta \\ v_a = v \times \cos\theta + u \times \sin\theta \end{cases} \tag{4}$$

where u and v are the zonal and the meridional components of the velocity, respectively, and θ is the angle of the coastal line from the east, which is about $60°$ in our study area. Since the isobaths offshore are almost parallel to the coastal line, we take the same θ as $60°$ at all stations for the decomposition as shown in Figure 1c.

2.6. Determination of Nutrients and Chlorophyll

The nutrient concentrations were measured using the San++ automated wet chemistry analyzer (Skalar, the Netherlands). The water sample analysis followed the *methods of sea water analysis* [42]. Nitrate, phosphate, and silicate were determined by the cadmium–copper column reduction method, phosphorus molybdenum blue method, and silicon molybdenum blue method, respectively. The detection limits were 0.1, 0.03, and 0.1 $\mu mol/dm^3$ for NO_3^-/NO_2^-, PO_4^{3-}, and SiO_3^{2-}, respectively. Millipore ultrapure water was used for on-site measurement and reagent preparation.

The determination of a concentration of chlorophyll was carried out by the fluorescence method in *Specifications for oceanographic survey* [43]. The filter was placed in a stoppered test tube, and 10 mL of 90% acetone (analytical grade) was added. The mixture was extracted in a low-temperature ($-20\,°C$) refrigerator for 24 h and the extract was taken to detect the fluorescence value on the Turner Designs Model 10-AU Fluorometer. The chlorophyll a concentration is calculated by the following formula:

$$\text{Chl } a = F_d \times [r/(r-1)] \times (R_b - R_a) \times (V_1/V_2) \tag{5}$$

where the concentration of Chl a in seawater is in $\mu g/L$, F_d is the conversion factor of range d in $\mu g/L$, R_b is the fluorescence value before acidification, R_a is the fluorescence value after acidification, r is the pure chlorophyll (purchased sample) acidification ratio, V_1 is the volume of the extract in mL, and V_2 is the water sample filtration volume in mL [40].

2.7. Volume and Nutrient Fluxes

The volume and nutrient fluxes are calculated using the velocity through a section, i.e.,

$$Q_v = \int_0^l \int_{-H}^0 V\,dz\,dl, \tag{6}$$

$$F = \int_0^l \int_{-H}^0 c \cdot V \, dz \, dl, \tag{7}$$

where Q_v and F are the volume flux and the nutrient flux, respectively, V is the velocity v_c or v_a, and c is the concentration of nutrient. The integral limit l is the section length and H is the depth. For calculation, the velocity and nutrient profiles were extrapolated to the surface and the bottom using the nearest observed data. Specifically, the velocities near the surface are filled with the topmost observations, while the velocities below the last observed bins are assumed to decrease linearly to zero at the ocean bottom (no-slip boundary condition). The nutrient profiles are extended to the surface and the bottom with constant values as those in the observed first and last values.

3. Results

3.1. Wind Analysis

Figure 2a–e shows the distribution of mean sea surface winds in the study area in the cases without the typhoon on 13 and 15–17 July 2012, before the typhoon on 31 July 2013, during the typhoon on 2 August 2013, and after the typhoon on 5 and 8 August 2013, respectively. One can see that the wind in the case without the typhoon was southwesterly in July 2012 as the climatological summer wind in this area (Figure 2a) [44], while the wind direction turned west–northwestward in the case before the typhoon on 31 July 2013 (Figure 2b). When the typhoon was coming on 2 August 2013 (Figure 2c), the cyclonic circulation appeared in the offshore area northwestward over the observation sections. In the case after the typhoon, the wind returned southeastward on 5 August (Figure 2d) and then increased to become a strong southeasterly wind over the whole area on 8 August (Figure 2e). The typhoon disturbed the wind field significantly in the study area east of Hainan Island.
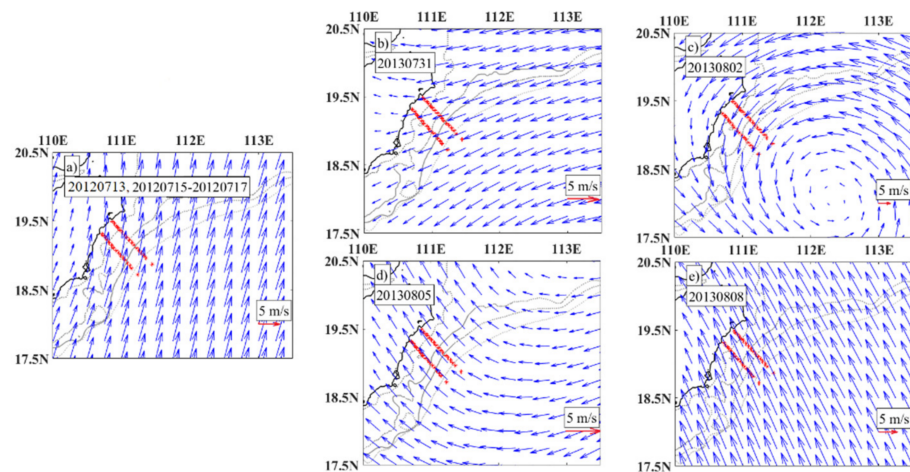

Figure 2. Sea surface wind vectors (blue arrows) in the case without the typhoon on 13 and 15–17 July 2012 (**a**), before the typhoon on 31 July 2013 (**b**), during the typhoon on 2 August 2013 (**c**), and after the typhoon on 5 (**d**) and 8 August 2013 (**e**). Red stars represent observation stations in the two sections H and F. Gray lines represent isobaths of 50, 100, 150, and 200 m.

3.2. Changes in Current Field

3.2.1. Tidal Currents

The total tidal velocities composed of the main tidal components (M_2, S_2, N_2, K_2, K_1, and O_1) at the observation time derived from the model TPXO are shown in Figure 3. One can see that in the case without the typhoon (Figure 3a), the tidal flow orientation was mostly along-shore within the 100 m isobath with the maximum speed of 0.04 m/s, and in east–west direction in the region beyond 100 m isobaths with a velocity larger than 0.02 m/s. In the case before the typhoon (Figure 3b), the tidal velocity of section H was

from 0.01 to 0.03 m/s. In the case after the typhoon (Figure 3c), the tidal flow speed was within a range of 0.02–0.04 m/s because of the spring tide. In all the cases, the observed total current velocities (obtained from the ADCP) are one order of magnitude larger than that of the tidal flow. Thus, the tidal effects on the volume and nutrient transports are insignificant.
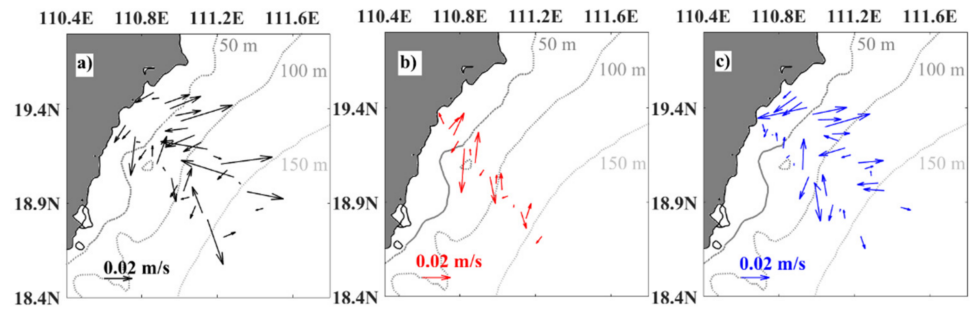

Figure 3. Distributions of tidal flow vectors without the typhoon (**a**), before the typhoon (**b**), and after the typhoon (**c**). Gray dashed lines represent isobaths.

3.2.2. De-Tided Velocity Fields

The current fields after de-tided processing (i.e., the observed total current velocities minus tidal velocities) are shown in Figure 4. Compared with the total velocity from the ADCP measurements, the patterns and values of current fields have little change, so the total velocity is not shown here. In the 15 m layer (Figure 4a), the case without the typhoon (black arrows) shows the northeastward flow with top velocity reaching 0.4 m/s and reducing to 0.2 m/s at the 100 m isobath. In the case before the typhoon (blue arrows), the offshore flow vectors were southwestward with amplitudes smaller than 0.2 m/s. The flow between the 50 m and 100 m isobaths was northeastward with the velocity within a range of 0.2–0.3 m/s. The flow turned northwestward with the velocity of about 0.2 m/s in the area deeper than 100 m. In the case after the typhoon (red arrows), the flow direction was almost opposite to that in the case before the typhoon, and the velocities increased to 0.5 m/s.
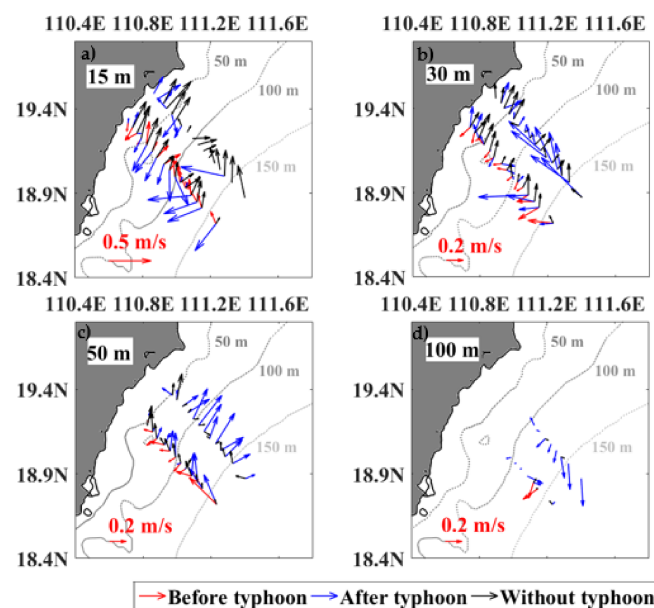

Figure 4. Distributions of current velocities after de-tided processing at a depth layer of 15 m (**a**), 30 m (**b**), 50 m (**c**), and 100 m (**d**). Gray dashed lines represent isobaths of 50, 100, and 150 m.

At a depth of 30 m (Figure 4b), the case without the typhoon shows the flow to be northeastward, but shoreward in the region beyond the 120 m isobath. In the case before the typhoon, the velocity significantly reduced compared with that in the case without the typhoon, and the flow direction reversed southwestward or westward. In the case after the typhoon, the near-shore flow orientation was almost opposite to that before the typhoon. The flow patterns of section H beyond the 120 m isobath were similar to the case before the typhoon, while F section is dominated by a northwestward flow with a speed greater than 0.5 m/s, while the speed in section H is less than in section F.

At a depth of 50 m (Figure 4c), in the case without the typhoon, the directions are more shoreward as its upper layers while the velocities are decreased to 0.1 m/s. In the case before the typhoon, on the one hand, one can see that the direction becomes more shoreward than upper layers and, on the other hand, the velocities become larger with the distance from the coastline increasing. In the case after the typhoon, section F was dominated by northeastward 0.4 m/s flow, while the velocities in section H were about 0.2 m/s.

At a depth of 100 m (Figure 4d), the velocity was 0.05 m/s offshoreward in the case without the typhoon, and raised to 0.2 m/s southwestward in the case before the typhoon. This situation is the same as the case after the typhoon. In the area deeper than 120 m, the speeds became greater, and the speeds in section F were greater than those in section H, with the maximum value of 0.3 m/s.

3.2.3. Along-Shore and Cross-Shelf Currents

The Along-Shore Component v_a

The along-shore velocities of section F and section H in the three cases are shown in Figure 5. The positive values represent the northeastward velocity. To simply description, we divide the whole section into five portions by red dotted lines. Horizontally, the first red dotted line is 23 km from the coast, within the 50 m isobath, and the second is 67 km from the coast, within the 120 m isobath. Vertically, the dotted line represents the depth of 50 m. The five portions represent the offshore water (OSW), the upper and subsurface layer of the shallow shelf water (SSW), as well as the upper and subsurface layer of the deep shelf water (DSW), respectively. One can see that in the case without the typhoon, the along-shore velocities in section H and section F (Figure 5a,d) are mainly northeastward in all the five portions except some regions below 50 m. There were weak southwestward flows < −0.1 m/s in the subsurface layer of the SSW and DSW. The mean speed reached the maximum in the OSW, and decreased downward and offshore. At the same time, in the case before the typhoon (Figure 5b), the flows turned to the opposite direction in section H, except for the upper 20 m in the SSW and the subsurface layer in the DSW. In the case after the typhoon (Figure 5c,e), the surface currents in the OSW and the upper SSW turned to the inverse directions again in section H. Moreover, the velocities in the DSW were enhanced for one order of magnitude greater than those in the case before the typhoon. In the upper 50 m, the maximum southwestward flow was beyond −0.5 m/s. On the contrary, in the lower layer the northeastward countercurrent also reached 0.4 m/s, implying a strong vertical shear flow. Section F was short of data in the case before the typhoon. In the case after the typhoon, the current directions were similar in sections F and H, and the vertical shear in section F was stronger than that in section H.

Cross-Shelf Component v_c

The two-dimensional (2D, *x–z*) distributions of the cross-shelf component in the three cases are shown in Figure 6. The positive values represent the offshore, southeastward flows. In the case without the typhoon (Figure 6a,b), one can see that the study area was basically dominated by negative, onshore flows from −0.1 to −0.3 m/s. In section F, there was a weak, offshore flow < 0.1 m/s between 50 m and 120 m isobaths. In the case before the typhoon (Figure 6b), the flow turned to be positive, offshoreward 0.1 m/s in the OSW in section H. The flows in other portions reach a maximum value of −0.4 m/s. In the case

after the typhoon, in section H (Figure 6c), the onshore flows were dominant, except for the offshore flows at the upper 30 m of the SSW and in the subsurface layer of the DSW. In section F (Figure 6e), there was a strong velocity shear at 50 m.
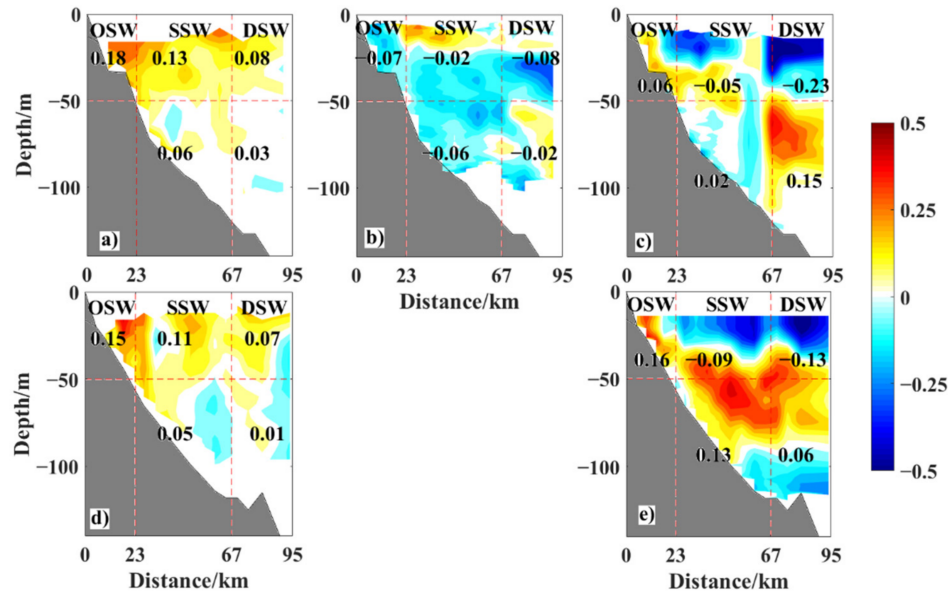

Figure 5. Two-dimensional (2D, *x*–*z*) distribution of the along-shore velocity component v_a (m/s) in section H (**a**) and F (**d**) without the typhoon, section H (**b**) before the typhoon, and sections H (**c**) and F (**e**) after the typhoon. Red dotted lines represent the positions of the 50 m isobath, the 120 m isobath, and a depth of 50 m. Numbers represent the average velocities in the portions of waters.
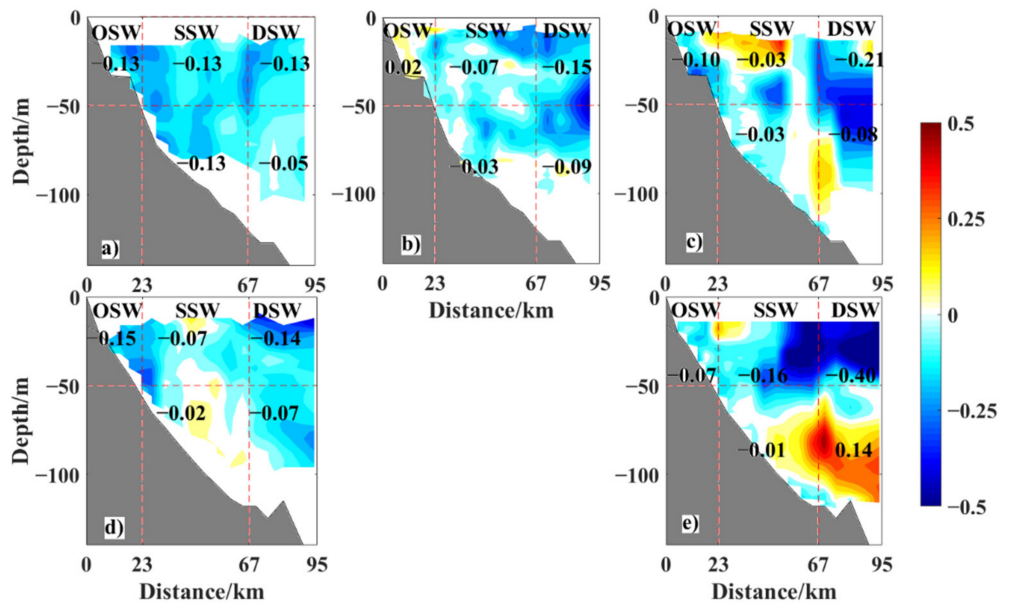

Figure 6. 2D (*x*–*z*) distributions of cross-shelf velocity components v_c (m/s) in section H (**a**) and F (**d**) without the typhoon, section H (**b**) before the typhoon, and sections H (**c**) and F (**e**) after the typhoon. Red dotted lines represent the positions of the 50 m isobath, the 120 m isobath, and a depth of 50 m. Numbers represent the average velocities in the portions of waters.

3.3. Changes in Nutrient and Chl a

3.3.1. Distribution of Concentrations

Figure 7 shows the distributions of Chl a and nutrient concentrations, which are linearly interpolated to 1 m intervals in depth. There were nutrient observations at depths ranging from 5 to 30 m at stations H3 to H5 in the OSW, H9 to H11 in the SSW, and H14 to H15 in the DSW in the case without the typhoon (Figure 7a,d,g,j). One can see that the concentration of NO_3^- (Figure 7a) decreased with the depth, and that it was higher in the DSW than that in the OSW, in which the maximal concentration reaches 5 μmol/L. The concentration of NO_2^- (Figure 7d) in the upper 20–30 m layer in the OSW and SSW reached the maximum of 0.35 μmol/L. In the OSW, the concentration increased with increasing depth. The concentration of PO_4^{3-} increased with depth and decreased with the distance from the coast. The peak value was beyond 0.4 μmol/L. The distribution patterns of SiO_3^{2-} (Figure 7j) were similar to those of PO_4^{3-}. The maximal concentration in the subsurface layer in the OSW reached 8 μmol/L, while the concentration of about 3 μmol/L was relatively homogeneously distributed in the 5–15 m layer.

In the case before the typhoon, the nutrient data were available only at stations H1–H4 in the OSW as shown in Figure 7b,e,h,k,m. One can see that the distribution patterns of NO_3^-, NO_2^-, and PO_4^{3-} were almost the same, i.e., the concentrations increased with depth and decreased with the distance from the coast in the OSW. The concentration ranges of NO_3^-, NO_2^-, and PO_4^{3-} are 0.5–2.5, 0.3–0.7, and 0.15–0.4 μmol/L, respectively. In the surface layer, SiO_3^{2-} (Figure 7k) and Chl a (Figure 7m) reached the peak values of 7 μmol/L and 2.5 μg/L, respectively. Meanwhile, they all decreased offshoreward and downward, but the concentration of SiO_3^{2-} increased near the bottom.

In the case after the typhoon, observation data are available at stations H1 and H4 in the OSW, H8, H10, H12, and H13 in the SSW, and H15 and H16 in the DSW, as shown in Figure 8c,f,i,l,m. One can see that the distribution patterns of NO_3^- (Figure 7c), PO_4^{3-} (Figure 7i), and SiO_3^{2-} (Figure 7l) are similar, i.e., the deeper the water, the higher the concentration. It should be noted that the concentration of SiO_3^{2-} started to increase at 70–80 m, while those of the other two at 50 m. In the bottom layer, the high concentration nutrient waters climb along the shelf break. The concentration of NO_2^- (Figure 7f) was uniform over 30 m and under 80 m and reached a peak value near a depth of 50 m 23 km from the coast. The concentration of Chl a (Figure 7n) decreased from OSW to SSW. Higher concentrations appear in the OSW and the bottom of the SSW. According to the previous investigations, typhoon rainfall strengthens the runoff with rich terrestrial nutrients. This results in an increase in the Chl a concentration in the OSW [30,45]. At the bottom 40 km from the coast, the chlorophyll a concentration reaches a maximum of 0.8 μmol/L.

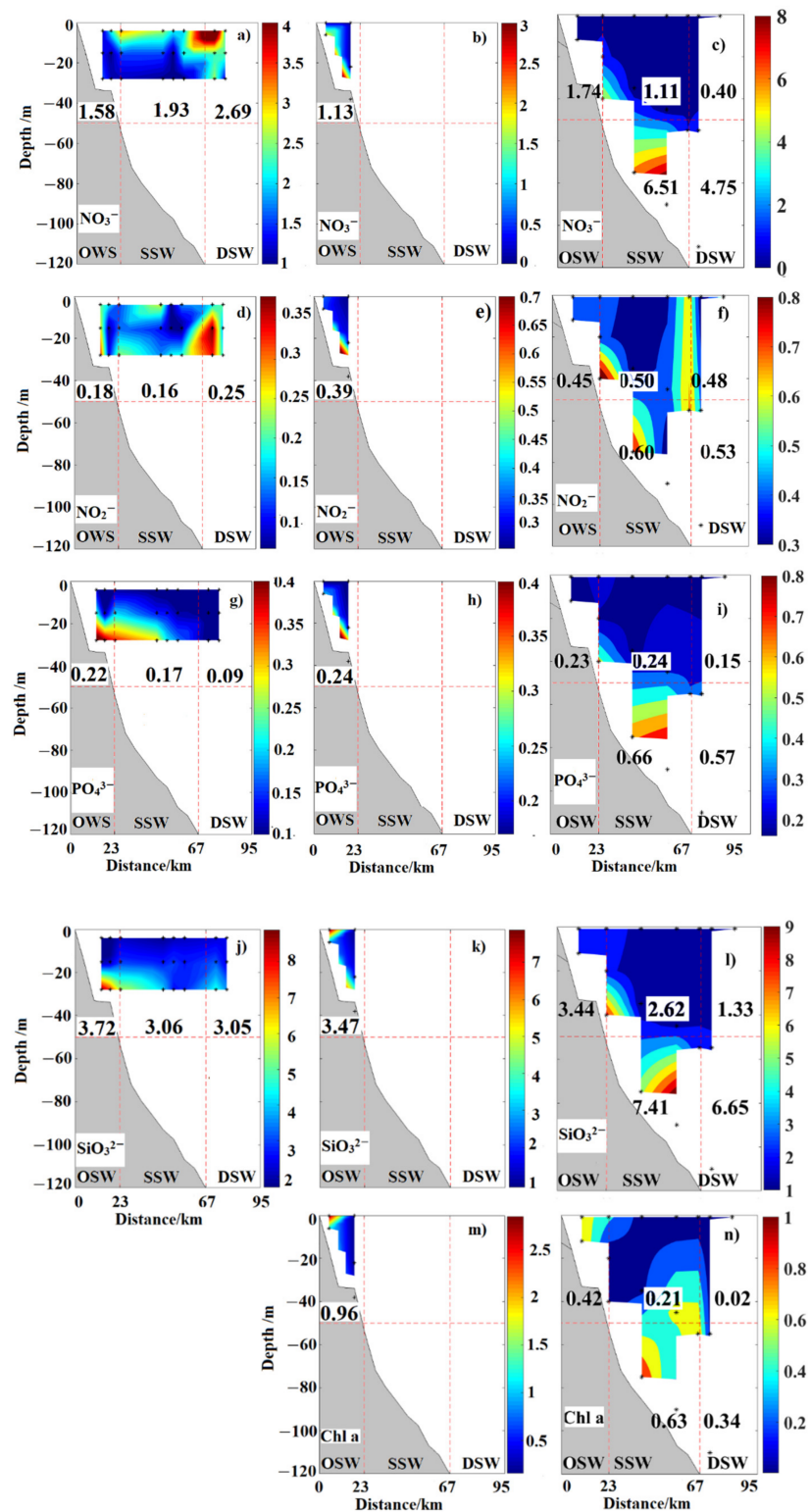**Figure 7.** 2D (*x–z*) distributions of nutrient and Chl a concentrations. (**a**,**d**,**g**,**j**) Without the typhoon (Stations H3–H5, H9–H11, and H14–H15). (**b**,**e**,**h**,**k**,**m**) Before the typhoon (Stations H1–H4). (**c**,**f**,**i**,**l**,**n**) After the typhoon (Stations H1, H4, H8, H10, H12–H13, and H15–H16). Dotted red lines represent the positions of 50 m and 150 m isobaths and a depth of 50 m. Black stars represent stations and depths of the observations. Numbers represent the average concentrations.
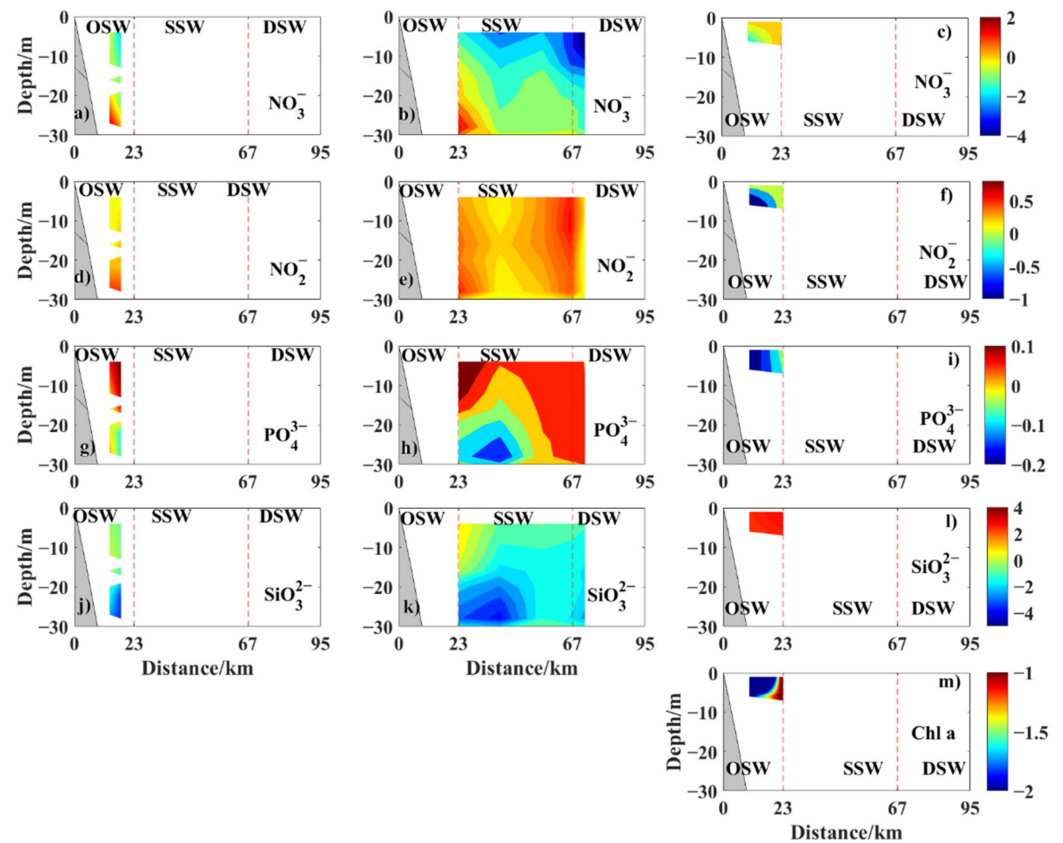
Figure 8. 2D (*x–z*) distributions of variations of nutrient and Chl a concentrations. (**a**,**d**,**g**,**j**) are for before the typhoon–without the typhoon, (**b**,**e**,**h**,**k**) for after the typhoon–without the typhoon, and (**c**,**f**,**i**,**l**,**m**) for after the typhoon–before the typhoon. Dotted red lines represent positions of 50 m and 120 m isobaths.

3.3.2. Variations of Concentrations

Figure 8 shows the difference between nutrient distributions derived from available data in the three cases: (1) before the typhoon–without the typhoon, (2) after the typhoon–without the typhoon, and (3) after the typhoon–before the typhoon. In the case (1), one can see that the concentrations of NO_3^- (Figure 8a) in the OSW decreased at the upper 15 m and increased to 1 μmol/L at the bottom, while the concentration of NO_2^- increased to about 0.1 to 0.4 μmol/L from surface to bottom, respectively. However, PO_4^{3-} (Figure 8g) went in a reversed direction from that of NO_3^-, in that its concentration increased to 0.1 μmol/L at the upper 15 m, while it decreased a little below 15 m. The concentration of SiO_3^{2-} (Figure 8j) decreased to 0.5 μmol/L at the upper layer and to 2 μmol/L below 15 m.

In case (2), the concentration of NO_3^- (Figure 8b) in the surface layer decreased in the case after the typhoon, and the difference became larger with distance from the coast, with the maximum value reaching −4 μmol/L. Below 20 m, the concentration of NO_3^- increased after the typhoon, with the maximal increment of 2 μmol/L. Opposite to the variation of NO_3^-, the concentrations of PO_4^{3-} (Figure 8h) and SiO_3^{2-} (Figure 8k) increased at a depth of 5–10 m in the OSW but decreased below a depth of 10 m. Nonetheless, the concentration of NO_2^- (Figure 8e) increased below a depth of 30 m.

In case (3), the concentrations of NO_3^- (Figure 8c), NO_2^- (Figure 8f), PO_4^{3-} (Figure 8j) and and Chl a (Figure 8m) in OSW mostly decrease in the 5 m layer within 10 km offshore and increase in deeper stations in the OSW, except that SiO_3^{2-} (Figure 8l) mostly increases.

3.4. Volume and Nutrient Transports

3.4.1. Volume Transport

The calculated results of volume transports in the layers above and below 50 m are shown in Figure 9. One can see three-dimensional (3D) distribution patterns of volume transport fluxes in the three cases: without the typhoon, before the typhoon, and after the typhoon.
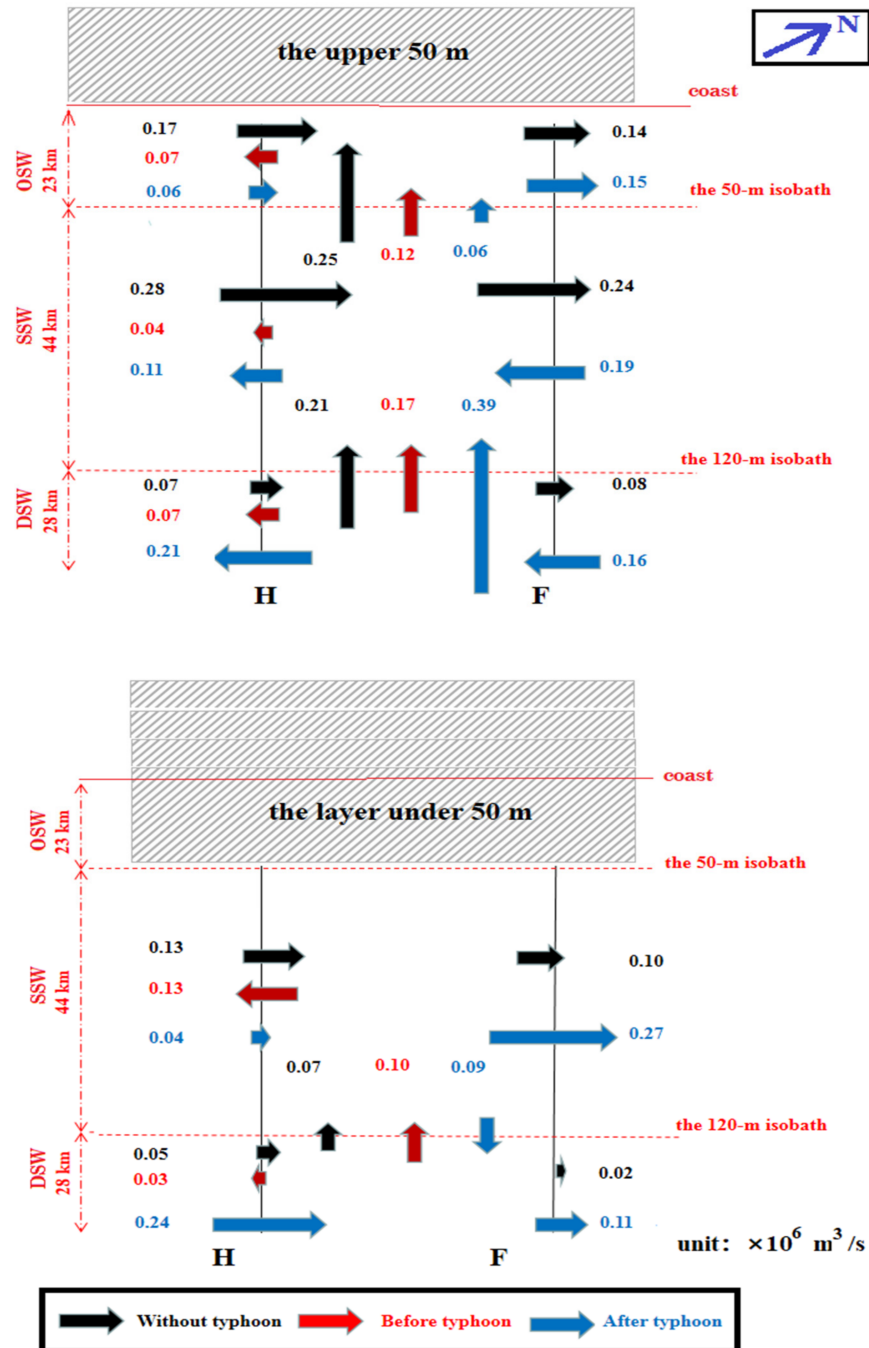

Figure 9. Diagram of volume transports.

In the case without the typhoon, the total along-shore fluxes (black arrows) of sections H and F at the upper 50 m were 0.52×10^6 m^3/s (0.17×10^6 m^3/s in OSW + 0.28×10^6 m^3/s in SSW + 0.07×10^6 m^3/s in DSW) and 0.46×10^6 m^3/s (0.14×10^6 m^3/s in OSW + 0.24×10^6 m^3/s in SSW + 0.08×10^6 m^3/s in DSW), respectively. The transports in SSW

from 50 m to 120 m isobaths had the largest values of 0.28×10^6 m^3/s and 0.24×10^6 m^3/s of sections H and F, respectively. Below a depth of 50 m, the total volume transport was 0.18×10^6 m^3/s (0.13×10^6 m^3/s in SSW + 0.05×10^6 m^3/s in DSW) crossing section H and 0.12×10^6 m^3/s (0.10×10^6 m^3/s in SSW + 0.02×10^6 m^3/s in DSW) crossing section F, respectively. Furthermore, the onshore transport at the upper 50 m was -0.21×10^6 m^3/s (shoreward) crossing the 120 m isobath, and it increased to -0.25×10^6 m^3/s when crossing the 50 m isobath. Below 50 m, the onshore transport was -0.07×10^6 m^3/s.

Compared with the case without typhoon, at the upper 50 m, the along-shelf flux direction was reversed in the whole section in the case before the typhoon, and the fluxes in the OSW and SSW were 41% and 14% of the absolute values in the case without the typhoon. The flux in the DSW was equivalent to the absolute value in the case without the typhoon. Below 50 m, the total along-shore transport was -0.16×10^6 m^3/s, with the direction opposite to that in the case without the typhoon. In the cross-shelf direction, the DSW inputs -0.17×10^6 m^3/s shoreward at the 120 m isobath, 81% of that in the case without the typhoon, while the transport in OSW is -0.12×10^6 m^3/s, 48% of that in the case without the typhoon. Below 50 m, the onshore transport is -0.10×10^6 m^3/s at the 120 m isobath.

In the case after typhoon (blue arrows), the along-shore flux direction was the same as that in the case without the typhoon in the OSW, but opposite to that before the typhoon. The transport value was even a little larger than that in the case without the typhoon. In the SSW and DSW, the along-shore fluxes were opposite to that in the case without the typhoon and the mean values were -0.15×10^6 m^3/s and -0.19×10^6 m^3/s, respectively. Below 50 m, the along-shelf flux direction was the same as that in the case without the typhoon. The total flux of section F was 0.38×10^6 m^3/s (0.27×10^6 m^3/s in SSW and 0.11×10^6 m^3/s in DSW), which was 0.10×10^6 m^3/s greater than that of section H (0.28×10^6 m^3/s total, 0.04×10^6 m^3/s in SSW, and 0.24×10^6 m^3/s in DSW). For the cross-shelf transport, it was -0.06×10^6 m^3/s onshore at the 50 m isobath and -0.39×10^6 m^3/s at the 120 m isobath. Combined with the increased along-shore transport in section F, one can see that there is a convergence zone within the two isobaths, indicating downwelling there. In the layer below 50 m, the flux across the 120 m isobath reversed seaward with a transport of 0.09×10^6 m^3/s.

3.4.2. Nutrient Transports
Along-Shore Fluxes

Figure 10 shows along-shore nutrient fluxes derived from available nutrient data measured at the upper 50 m of section H. One can see one-dimensional (1D) distribution patterns of nutrient transport fluxes in the three cases: without the typhoon, before the typhoon, and after the typhoon.

In the case without typhoon, the along-shore nutrient fluxes (no data for Chl a) were northeastward, and the maximum values appear in the SSW as the volume transport. The total fluxes across the section were 10.2×10^8, 9.52×10^7, 9.32×10^7, and 17.2×10^8 μmol/s for NO_3^-, NO_2^-, PO_3^{4-}, and SiO_3^{2-}, respectively. In the case before the typhoon, all the fluxes in OSW (only available) were reversed and smaller than those in the case without the typhoon, except booming Chl a. In the case after typhoon, the flux of NO_3^- in the OSW had the same direction as, but 36% of the magnitude of, that in the case without the typhoon, while in the SSW and DSW, the fluxes are reversed with 19% and 45% of magnitudes of that in the case without typhoon. The fluxes of NO_2^-, PO_3^{4-}, and SiO_3^{2-} showed similar behavior to that of NO_3^-, but enhanced magnitudes as high as 5.5, 1.9 and 1.3 times in the DSW, respectively. However, the flux of Chl a in the OSW decreased to 37% of that in the case before the typhoon.
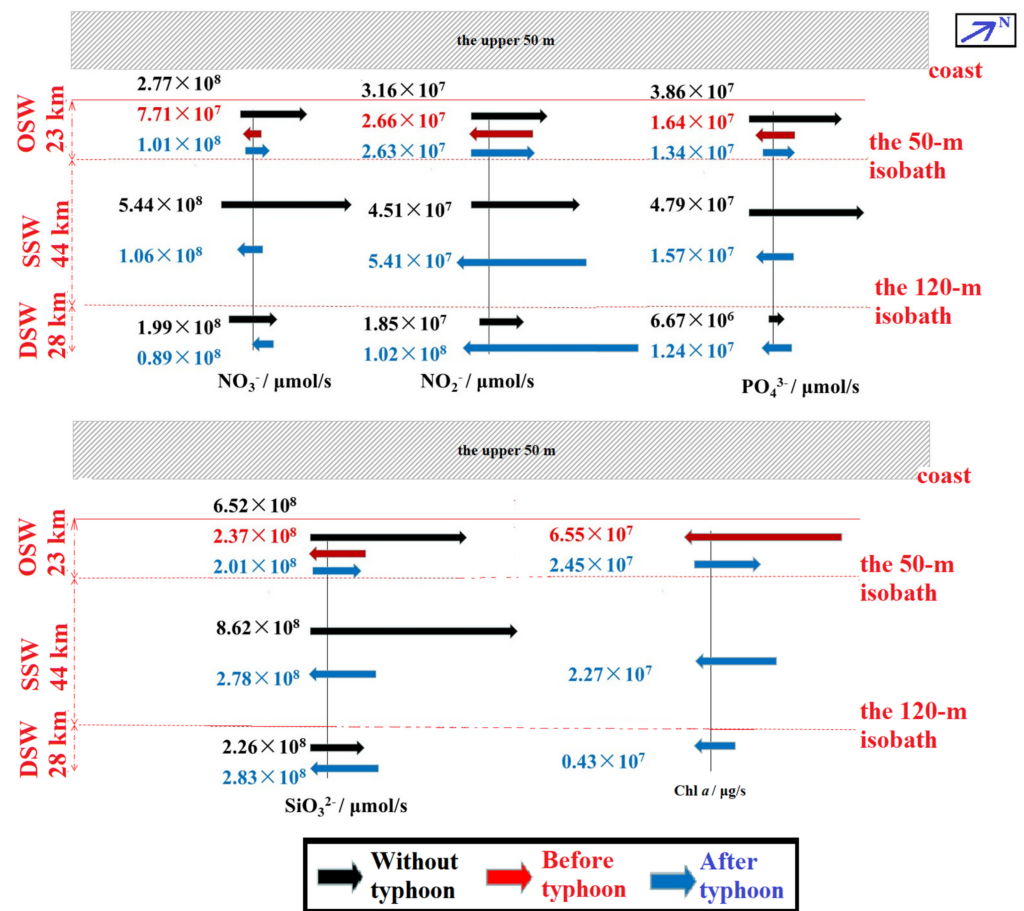
Figure 10. Diagram of nutrient fluxes in the upper 50 m.

The averaged along-shore nutrient fluxes per unit area in OSW across the section in the upper 50 m are listed in Table 1. The positive direction is northeastward. One can see that, in general, the fluxes turn to the opposite direction and decrease the magnitudes by more than half except NO_2^- in the case before the typhoon compared to that in the case without the typhoon. In the case after the typhoon, the averaged along-shore nutrient fluxes recover to positive directions as those in the case the without typhoon, but the magnitudes are three times smaller than those in the case without the typhoon expect NO_2^-.

Table 1. Averaged along-shore nutrient fluxes per unit area in the offshore water (OSW).

	NO_3^- (μmol/s)	NO_2^- (μmol/s)	PO_4^{3-} (μmol/s)	SiO_3^{2-} (μmol/s)	Chl a (μg/s)
Without the typhoon	367.31	41.10	51.73	866.13	N/A
Before the typhoon	−104.52	−39.83	−24.11	−292.93	−61.03
After the typhoon	134.07	34.21	17.96	267.01	11.30

Cross-Shelf Fluxes

The averaged cross-shelf nutrient fluxes per unit area in OSW along the section in the upper 50 m are listed in Table 2. The negative signs represent the onshore direction. One can see that the fluxes of all the nutrients are shoreward, but have different behaviors disturbed by the typhoon passage. Compared with values in the case without the typhoon, the averaged fluxes of PO_4^{3-} in the cases before and after the typhoon were reduced to 1/2 and of SiO_3^{2-} were reduced to 1/3, while those of NO_3^- decreased to 1/5 and 1/2, respectively. The fluxes of NO_2^- in the cases before and after the typhoon changed little.

The flux of Chl a decreased by 81% in the case after the typhoon in comparison to that in the case before the typhoon.

Table 2. Cross-shelf nutrient fluxes per unit area in OSW.

	NO_3^- (μmol/s)	NO_2^- (μmol/s)	PO_4^{3-} (μmol/s)	SiO_3^{2-} (μmol/s)	Chl a (μg/s)
Without the typhoon	−341.18	−27.92	−39.70	−632.74	N/A
Before the typhoon	−73.16	−36.77	−21.28	−228.25	−20.54
After the typhoon	−153.33	−22.58	−11.33	−239.61	−3.89

4. Discussion

4.1. Impacts of Tidal Current on Calculated Results

In our research region, the observed current velocity data contain the tidal current components. To remove the influence of the tidal currents, we use the TPXO mode to calculate barotropic tides at the observation station and remove them from the observed current data, as shown in Figure 4. Tables 3 and 4, respectively, compare the averaged cross-shelf and along-shore volume flux per unit area before and after de-tided processing. It is evident that the observed total current velocities (obtained from the ADCP) are one order of magnitude larger than that of the tidal flow, and the influence of the barotropic tides on the volume flux is negligible, expect in the case after the typhoon for section F. On the one hand, the results of pioneers [46,47] indicate that the tidal current velocity in this area is usually 0.1 m/s, while the observed maximum current velocity exceeds 0.5 m/s, implying that the contribution of the baroclinic tidal current to the total velocity is small. On the other hand, the time spent on the observation of a section is one day (the tidal constituent of this area is M2), so the tidal current flux can be ignored in the total flux calculation. Of course, more observations and studies about the effects of baroclinic tides are worth pursuing.

Table 3. The along-shore water flux per unit area (before de-tided processing/after de-tided processing).

	Section H (m/s)	Section F (m/s)
Without the typhoon	0.09/0.09	0.07/0.07
Before the typhoon	−0.05/−0.05	N/A
After the typhoon	0.01/0.01	0.02/0.01

Table 4. The cross-shelf water flux per unit area (before de-tided processing/after de-tided processing).

	Section H (m/s)	Section F (m/s)
Without the typhoon	−0.11/−0.11	−0.07/−0.07
Before the typhoon	−0.06/−0.06	N/A
After the typhoon	−0.05/−0.05	−0.05/−0.07

4.2. Volume Balance

As shown in Figure 9, in the case without the typhoon, the volume entering OSW is much larger than output. As known in Section 4, the velocities near the surface are close to the topmost observations. According to the situation, the speculation is that the surface velocities are not close to the topmost observation and, thus, cause large errors and unbalance in volume.

In the case after the typhoon, the onshore cross-shelf transport across the 120 m isobath is -0.39×10^6 m^3/s, directly leading to the water convergence in SSW in upper the 50 m, with the value being about 0.41×10^6 m^3/s (the positive value represents

convergence), while below 50 m, the northeastern along-shore transport across section F, about 0.27×10^6 m^3/s, induces water divergence, which is -0.32×10^6 m^3/s. The hypothesis of Liu et al. [18] is that the unbalance in revenue and expenditure among two sections goes out in the horizontal direction, vertical to the section. Therefore, according to this hypothesis, our speculation is that the water in the upper 50 m sinks and then outputs along the shelf and reaches balance.

Vertical fluxes may also be important for the volume budget. Xie et al. [29] derived the 3D vertical velocities in the study area in the case without the typhoon using the Omega equation and 3D observations. Zheng [48] compared the diagnosed vertical velocity from one cross-shelf section to that from 3D observations and found that the two results are similar. This indicates that the vertical fluxes could be derived from the two sections. Further analysis of the nutrient budget with the vertical fluxes will give insight into the biological consumption process if the budget is not closed with the transport terms.

4.3. Physical Mechanism

In the case after the typhoon, one can see that not only the speed becomes large, but also the horizontal and vertical shear become large compared with the cases without and before the typhoon (Figures 5 and 6). It implies that enhanced mixing and instability might occur after the typhoon. From Figures 2 and 11, one can see that with an increase in the wind speed in the case during the typhoon (Figure 2c), the Ekman layer thickness D_E significantly increased, to over 80 m (Figure 11c), larger than the bottom depth in the OSW and SSW, indicating the strong and deep influence of the typhoon. In contrast, before the typhoon (Figure 11b) and just after the typhoon passage (Figure 11d), D_E was generally less than 40 m when the winds were weak (Figure 2b,d). After the typhoon passed far away and a strong southeasterly wind developed, D_E increased to more than 100 m (Figure 11e). Therefore, the current appeared to be in a sharp state in the case after the typhoon. For the cross-shelf current, with the effect of the onshore wind, the current appeared in the onshore flow at the upper layer and reversed at the subsurface [34]. For the along-shore current, on the one hand, the anticlockwise effect of the typhoon on the right side of the study region (Figure 2c) makes the upper layer component cause a southwest flow. On the other hand, due to a strong convergence, the flow in the subsurface layer is towards the storm track [28].
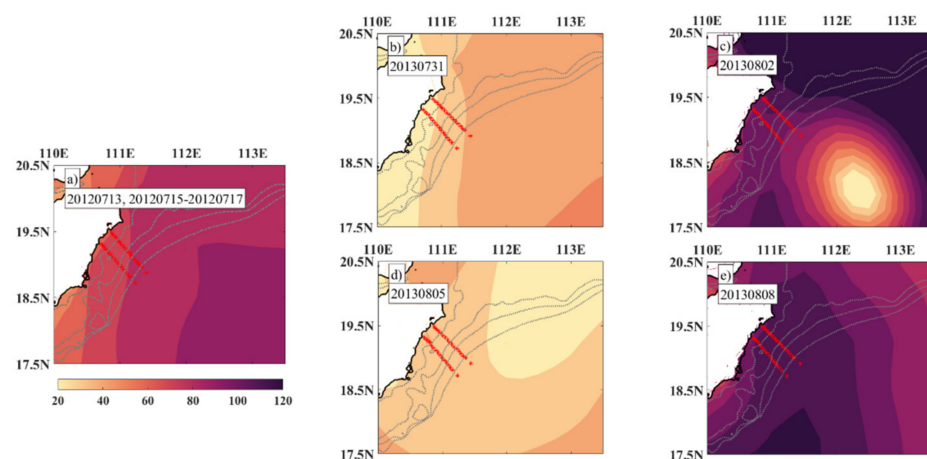

Figure 11. The Ekman layer thickness (m) in the case without the typhoon on 13 and 15–17 July 2012 (**a**), before the typhoon on 31 July 2013 (**b**), during the typhoon on 2 August 2013 (**c**), and after the typhoon on 5 (**d**) and 8 August 2013 (**e**). Red starts represent observation stations in the two sections H and F. Gray lines represent iso-baths of 50, 100, 150, and 200 m.

The along-shore and cross-shelf transports are also affected by the wind. Figure 12 shows the Ekman transports in the three cases: without, before, and after the typhoon. One can see that in the case without the typhoon, the transport was almost eastward

(Figure 12a) and the budget of measurement was balanced basically (Figure 9). In the case before the typhoon, the transport was northwestward (Figure 12b) with downwelling (Figure 13b). The state corresponds to the measurement transport. In the case after the typhoon, one can see that the transport was northwest (Figure 12c) with downwelling (Figure 13b). According to Figure 12c, the onshore transport by the typhoon is so large that the effect may last until the case after the typhoon. That's why the onshore volume is so large in Figure 9, while the cross-shelf component of the Ekman transport is weak and directed offshore. The upper 50 m transport was southwestward and the layer under 50 m was opposite. This situation also supports our supposition well.
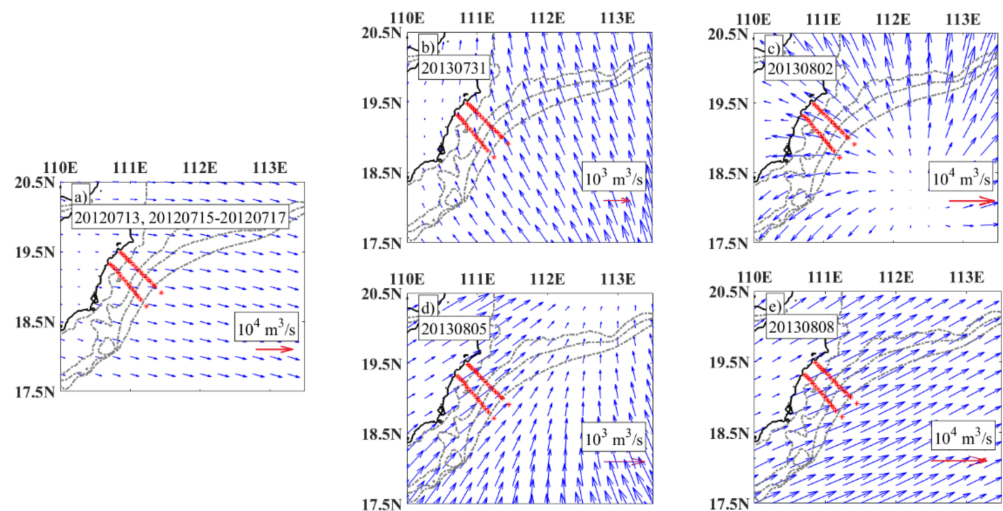

Figure 12. The Ekman transport in the case without the typhoon on 13 and 15–17 July 2012 (**a**), before the typhoon on 31 July 2013 (**b**), during the typhoon on 2 August 2013 (**c**), and after the typhoon on 5 (**d**) and 8 August 2013 (**e**). Red starts represent observation stations in the two sections H and F. Gray lines represent iso-baths of 50, 100, 150, and 200 m.
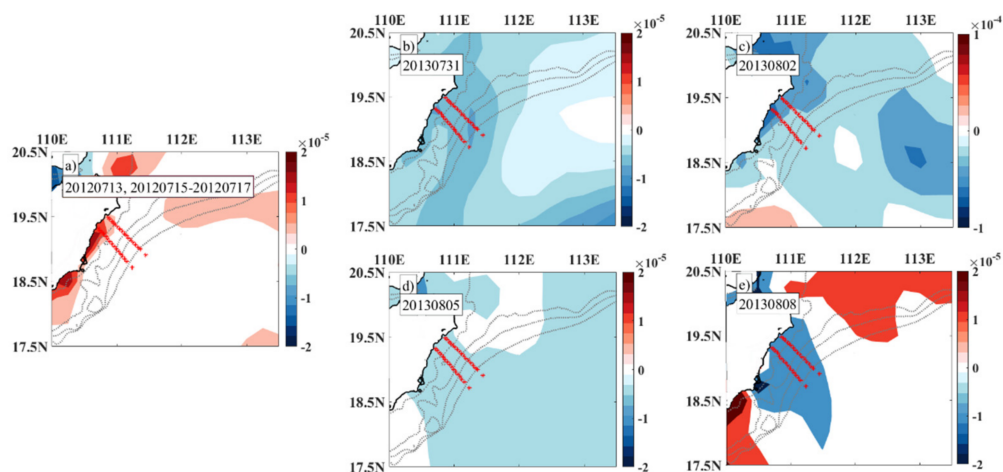

Figure 13. The Ekman pumping (m/s) in the case without the typhoon on 13 and 15–17 July 2012 (**a**), before the typhoon on 31 July 2013 (**b**), during the typhoon on 2 August 2013 (**c**), and after the typhoon on 5 (**d**) and 8 August 2013 (**e**). Red stars represent observation stations in the two sections H and F. Gray lines represent iso-baths of 50, 100, 150, and 200 m.

5. Conclusions

This study aims at understanding variations in the current structure and nutrient distributions under disturbance by typhoon passage over the coastal upwelling zone east

of Hainan Island, China. To conveniently describe the results, the study area is horizontally divided into three portions: the offshore water (OSW), within the 50 m isobath; the shallow shelf water (SSW), within the 50 m to 120 m isobaths; and the deep shelf water (DSW), beyond the 120 m isobath, from 67 to 96 km from the coastline, respectively. The along-shore and cross-shelf transports of volume and nutrients are calculated from cruise observations before and after the passage of the typhoon Chebi in August 2013 and without the typhoon in July 2012. The main findings are summarized as follows.

1.　In the case without the typhoon, the study area is controlled by the southwest monsoon. The current is mainly northeastward along the shore in the OSW and rotates counterclockwise to cross the shelf in the DSW and the deep layer below 50 m. The wind direction before the typhoon turns northeasterly. Meanwhile, the current direction changes into southwestward, starting from OSW to others, and velocity increases. In the case after the typhoon, the southerly winds prevail, and the current direction turns to be the same as that in the case without the typhoon. The vertical shear of horizontal velocity is greater than that in the case without the typhoon. There is water convergence near the 100 m isobath.

2.　In the case without the typhoon, the total along-shoreward volume transport mean is 0.64×10^6 m^3/s and the total cross-shelf transport mean is -0.28×10^6 m^3/s. In the case before the typhoon, however, the total along-shore transport is reversed southwestward and the average magnitude reduced to -0.34×10^6 m^3/s. The total cross-shelf transport mean is -0.27×10^6 m^3/s onshoreward, close to the value in the case without the typhoon. In the case after the typhoon, the total along-shore transport mean recovers to -0.09×10^6 m^3/s, while the total cross-shelf onshoreward transport mean increases by about 10% to -0.30×10^6 m^3/s.

3.　Compared with the along-shore nutrient fluxes in the case without the typhoon, in the case before the typhoon, all the fluxes in the OSW are reversed and smaller than those in the case without the typhoon, but Chl a is booming. In the case after the typhoon, the flux of NO_3^- in OSW has the same direction as, but decreases 64% in magnitude, while in the SSW and DSW, the fluxes are reversed and decrease 81% and 55% in magnitude, respectively. The fluxes of NO_2^-, PO_4^{3-}, and SiO_3^{2-} show similar behavior to that of NO_3^-, but have enhanced magnitudes, as high as 5.5, 1.9, and 1.3 times in DSW, respectively. However, the flux of Chl a in the OSW decreases to 37% of that in the case before the typhoon.

4.　Compared with the case without the typhoon, the typhoon passage, i.e., in the cases before and after the typhoon, greatly disturbs the distribution of nutrients. The averaged onshoreward transport fluxes in the OSW of NO_3^- decrease to 1/5 and 1/2, those of PO_4^{3-} in the two cases decrease to 1/2, and those of SiO_3^{2-} decrease to 1/3. On the contrary, the fluxes of NO_2^- in the two case changed little. Meanwhile, the onshoreward transport flux of Chl a decreases by 81% in the case after the typhoon in comparison to that in the case before the typhoon.

In conclusion, the results of this study indicate that typhoon passage may greatly disturb the circulation and the ecologic environment in the coastal upwelling zone east of Hainan Island, China. However, the effects on the behavior of nutrient elements differ. The mechanisms are worth pursuing in future efforts.

Author Contributions: M.Z.: data analysis; data interpretation; writing—original draft; L.X.: study design; data acquisition and interpretation; writing—review and editing. Q.Z.: writing—review. M.L., F.C. and J.L.: data acquisition. All authors have read and agreed to the published version of the manuscript.

References

1. Bauer, J.E.; Druffel, E.R.J.N. Ocean margins as a significant source of organic matter to the deep open ocean. *Nature* **1998**, *392*, 482. [CrossRef]
2. Cai, W.J.; Dai, M.; Wang, Y. Air-sea exchange of carbon dioxide in ocean margins: A province-based synthesis. *Geophys. Res. Lett.* **2006**, *33*, 347–366. [CrossRef]
3. Luo, X.F.; Wei, H. Progress on the study of continental shelf carbon cycle model. *Adv. Mar. Sci.* **2014**, *32*, 277–287.
4. Su, J.L. Strengthening the investigation and study of offshore China. *Adv. Earth Sci.* **1996**, *11*, 7–9.
5. Longhurst, A.; Sathyendranath, S.; Platt, T.; Caverhill, C. An estimate of global primary production in the ocean from satellite radiometer data. *J. Plankton Res.* **1995**, *17*, 1245–1271. [CrossRef]
6. Wei-Jun, C. Comment on "Enhanced open ocean storage of CO_2 from shelf sea pumping". *Science* **2004**, *306*, 1477c.
7. Brink, K.H. Cross-Shelf Exchange. *Annu. Rev. Mar. Sci.* **2016**, *8*, 59.
8. Hong, B.; Wang, D.X. Dynamic diagnosis of winter upwind in the northern South China Sea. *China Sci. Bull.* **2006**, *51*, 9–14. [CrossRef]
9. Fewings, M.; Lentz, S.J.; Fredericks, J. Observations of Cross-Shelf Flow Driven by Cross-Shelf Winds on the Inner Continental Shelf. *J. Phys. Oceanogr.* **2008**, *38*, 2358–2378. [CrossRef]
10. Qiao, L.L.; Wang, Z.; Liu, S.D.; Li, G.X.; Liu, X.; Huang, L.L.; Xue, W.J.; Zhong, Y. From continental shelf seas to the western Pacific: The path and mechanism of cross-shelf suspended sediment transport in the Yellow Sea and East China Sea. *Earth Sci. Front.* **2017**, *24*, 134–140.
11. Han, G. Three-dimensional seasonal-mean circulation and hydrography on the eastern Scotian Shelf. *J. Geophys. Res. Ocean.* **2003**, *108*, C53136. [CrossRef]
12. Herman, F.; Rhodes, E.J.; Braun, J.; Heiniger, L. Uniform erosion rates and relief amplitude during glacial cycles in the Southern Alps of New Zealand, as revealed from OSL-thermochronology. *Earth Planet. Sci. Lett.* **2010**, *297*, 183–189. [CrossRef]
13. Li, C. Cross-shelf passage of coastal water transport at the South Atlantic Bight observed with MODIS Ocean Color/SST. *Geophys. Res. Lett.* **2003**, *30*, 1257.
14. Yuan, D.; Zhu, J.; Li, C.; Hu, D. Cross-shelf circulation in the Yellow and East China Seas indicated by MODIS satellite observations. *J. Mar. Syst.* **2008**, *70*, 134–149. [CrossRef]
15. Dinniman, M.S.; Klinck, J.M. A model study of circulation and cross-shelf exchange on the west Antarctic Peninsula continental shelf. *Deep-Sea Res. Part II* **2004**, *51*, 2003–2022. [CrossRef]
16. Dong, S.H.; Liu, S.M.; Ren, J.L.; Li, J.; Zhang, J. Preliminary estimates of cross shelf transport flux of nutrients in the East China Sea in spring. *Mar. Environ. Sci.* **2016**, *35*, 385–391.
17. Wang, X.R.; Wang, Q.; Zhou, W.D.; Zhou, S.Q. Model diagnostic analysis of cross-shelf flow in the northern South China Sea. *Chin. Sci. Bull.* **2017**, *62*, 1059–1070.
18. Liu, J.; Dai, J.; Xu, D.; Wang, J.; Yuan, Y. Seasonal and Interannual Variability in Coastal Circulations in the Northern South China Sea. *Water* **2018**, *10*, 520. [CrossRef]
19. Deng, S.; Zhong, H.L.; Wang, M.W.; Yun, F.J. Upwelling along the coast of Qionghai and its relationship with fisheries. *J. Oceanogr. Taiwan Strait* **1995**, 51–56.
20. Jing, Z.; Qi, Y.; Du, Y.; Zhang, S.; Xie, L. Summer upwelling and thermal fronts in the northwestern South China Sea: Observational analysis of two mesoscale mapping surveys. *J. Geophys. Res. Ocean.* **2015**, *120*, 1993–2006. [CrossRef]
21. Xie, L.L.; Guo, X.S.; Zhang, Y.W.; Kang, J.J. Reference velocity from bottom track in LADCP data processing. *Ocean Technol.* **2013**, *32*, 34.
22. Chen, F.J.; Zeng, Z.; Meng, Y.F.; Zhu, Q.M.; Xie, L.L.; Zhang, S.W.; Chen, Q.X.; Chen, Q.X. Diel variation of nutrients and chlotophyll a concentration in the Qiongdong sea region during the summer of 2013. *Haiyang Xuebao* **2016**, *38*, 76–83.
23. Jing, Z.; Qi, Y.; Du, Y. Upwelling in the continental shelf of northern South China Sea associated with 1997–1998 El Niño. *J. Geophys. Res. Ocean.* **2011**, *116*, C02033. [CrossRef]
24. Xie, L.L.; He, C.F.; Li, M.M.; Tian, J.J.; Jing, Z.Y. Response of sea surface temperature to typhoon passages over the upwelling zone east of Hainan Island. *Adv. Mar. Sci.* **2017**, *35*, 8–19.
25. Xie, L.; Zong, X.; Yi, X.; Li, M. The interannual variation and long-term trend of Qiongdong upwelling. *Oceanol. Limnol. Sin.* **2016**, *47*, 43–51.

26. Zheng, M.L.; Li, M.M.; Xie, L.L.; Hong, Y.B.; He, Y.K.; Zong, X.L. Observational Analysis of Hydrographic Characteristics on the northwestern shelf of the South China Sea in winter 2012. *Oceanol. Limnol. Sin.* **2018**, *49*, 734–745.
27. Su, J.; Wang, J.; Pohlmann, T.; Xu, D. The influence of meteorological variation on the upwelling system off eastern Hainan during summer 2007–2008. *Ocean Dyn.* **2011**, *61*, 717–730. [CrossRef]
28. Tsai, Y.; Chern, C.S.; Wang, J. Numerical study of typhoon-induced ocean thermal content variations on the northern shelf of the South China Sea. *Cont. Shelf Res.* **2012**, *42*, 64–77. [CrossRef]
29. Xie, L.; Pallàs-Sanz, E.; Zheng, Q.; Zhang, S.; Zong, X.; Yi, X.; Li, M. Diagnosis of 3D vertical circulation in the upwelling and frontal zones east of Hainan Island, China. *J. Phys. Oceanogr.* **2017**, *47*, 755–774. [CrossRef]
30. Zhang, Y.; Tian, J. Enhanced turbulent mixing induced by strong wind on the South China Sea shelf. *Ocean Dyn.* **2014**, *64*, 781–796. [CrossRef]
31. Zheng, Z.-W. Unusual warming in the coastal region of northern South China Sea and its impact on the sudden intensification of tropical cyclone Tembin (2012). *Adv. Meteorol.* **2014**, *2014*, 250752. [CrossRef]
32. Guan, S.; Zhao, W.; Sun, L.; Zhou, C.; Liu, Z.; Hong, X.; Zhang, Y.; Tian, J.; Hou, Y. Tropical cyclone-induced sea surface cooling over the Yellow Sea and Bohai Sea in the 2019 Pacific typhoon season. *J. Mar. Syst.* **2021**, *217*, 103509. [CrossRef]
33. Pan, A.; Guo, X.; Xu, J.; Jiang, H.; Xiaofang, W. Responses of Guangdong coastal upwelling to the summertime typhoons of 2006. *Sci. China* **2012**, *55*, 495–506. [CrossRef]
34. Chang, Y.; Liao, H.T.; Lee, M.A.; Chan, J.W.; Lan, Y.C. Multisatellite observation on upwelling after the passage of Typhoon Hai-Tang in the southern East China Sea. *Geophys. Res. Lett.* **2008**, *35*, 154–175. [CrossRef]
35. Shi, Y.X.; Xie, L.L.; Li, M.M.; Wan, L.; Zheng, M.L.; Shen, Y.F. Impacts of Typhoon Mujigea on Sea Surface Temperature and Chlorophyll-a Concentration in the Coastal Ocean of Western Guangdong. *J. Guangdong Ocean Univ.* **2017**, *037*, 49–58.
36. Zhou, L.; Gao, S.; Yang, Y.; Zhao, Y.; Han, Z.; Li, G.; Jia, P.; Yin, Y. Typhoon events recorded in coastal lagoon deposits, southeastern Hainan Island. *Acta Oceanol. Sin.* **2017**, *36*, 37–45. [CrossRef]
37. Li, J.; Zheng, Q.; Li, M.; Li, Q.; Xie, L.L. Spatiotemporal Distributions of Ocean Color Elements in Response to Tropical Cyclone: A Case Study of Typhoon Mangkhut (2018) Past Over the Northern South China Sea. *Remote Sens.* **2021**, *13*, 687.
38. Yang, S.A.; He, L.F. Analysis of Atmosphere Circulation and Weather in August 2013. *Meteorol. Mon.* **2013**, *39*, 1521–1528.
39. He, C.F. Analysis of the Impact and Mechanism of Tropical Cyclone on the Thermocline Features of Qiongdong Upwelling. Master's Thesis, Guangdong Ocean University, Zhanjiang, China, 2016.
40. Zeng, Z. Seasonal and Diel Variation of Nutrients and Chlorophyll a Concentration in the Qiongdong. Master's Thesis, Guangdong Ocean University, Zhanjiang, China, 2015.
41. Egbert, G.D.; Erofeeva, S.Y. Efficient Inverse Modeling of Barotropic Ocean Tides. *J. Atmos. Ocean. Technol.* **2002**, *19*, 183–204. [CrossRef]
42. China National Standardization Management Committee. *Specifications for Oceanographic Survey—Part 4: Survey of Chemical Parameters in Sea Water*; China Standards Press: Beijing, China, 2007.
43. China National Standardization Management Committee. *Specifications for Oceanographic Survey—Part 6: Marine Biological Survey*; China Standards Press: Beijing, China, 2007.
44. Li, M.M.; Xie, L.L.; Zong, X.L.; Zhang, S.W.; Zhou, L.; Li, J.Y. The cruise observation of turbulent mixing in the upwelling region east of Hainan Island in the summer of 2012. *Acta Oceanol. Sin.* **2018**, *37*, 1–12. [CrossRef]
45. Zhao, H.; Tang, D.L.; Wang, D. Phytoplankton blooms near the Pearl River Estuary induced by Typhoon Nuri. *J. Geophys. Res.* **2009**, *114*, C12027. [CrossRef]
46. Wenping, G.; Jian, S.; Jianjun, J. Feedback between tidal hydrodynamics and morphological changes induced by natural process and human interventions in a wave-dominated tidal inlet: Xiaohai, Hainan, China. *Acta Oceanol. Sin.* **2009**, 96–116.
47. Wang, F.Y.; Qiu, L.G.; Liang, X.L.; Mo, W.Y.; Liang, N.A.; Wang, Y.Z. Response of human activities on tidal hydrodynamics of Hainan Qinglan tidal inlet system based on Delft 3D model. *Quat. Sci.* **2018**, *38*, 496–504.
48. Zheng, M.L. Seasonal Variability of 3D Volume and Nutrient Transports in the Northwestern South China Sea. Master's Thesis, Guangdong Ocean University, Zhanjiang, China, 2019.